




# A comparison of Ni, Pt, and NiPt catalysts supported on SBA-15 in anisole hydrodeoxygenation: Exploring the effect of platinum addition to a nickel catalyst

**Daniel E. Pérez-Estrada, Mitsuo A. Sernaqué-Villagómez, Luis H. Molina-Conde, and Alejandro Suárez-Méndez**, Facultad de Química, Universidad Nacional Autónoma de México (UNAM), 04510 Ciudad de México, Mexico

**Rubén Mendoza-Cruz** , Instituto de Investigaciones en Materiales, Universidad Nacional Autónoma de México (UNAM), Cd. Universitaria, Coyoacán, C.P. 04510 Ciudad de México, Mexico

**Tatiana E. Klimova** , Facultad de Química, Universidad Nacional Autónoma de México (UNAM), 04510 Ciudad de México, Mexico

Address all correspondence to Tatiana E. Klimova at [klimova@unam.mx](mailto:klimova@unam.mx)

(Received 14 November 2023; accepted 4 June 2024)

## Abstract

Ni, Pt, and NiPt catalysts supported on SBA-15 were synthesized, characterized, and tested in anisole hydrodeoxygenation to determine the effect of the metal's nature on the catalytic activity in the hydrogenation of the aromatic ring of anisole and hydrogenolysis of the C–O bond in the cyclohexyl methyl ether intermediate. Metal loadings in the catalysts were 5 wt% of Ni and 1 wt% of Pt. The bimetallic NiPt/SBA-15 catalyst showed the highest catalytic activity in both hydrogenation and hydrogenolysis, attributed to the promotional effect of Pt on NiO reduction and the formation of a Ni–Pt alloy with better dispersion of metal nanoparticles.

## Introduction

In recent years, the global demand for energy is in continuous increase, being petroleum the main source for energy production.<sup>[1]</sup> On the other side, the reduction in the use of fossil fuels and their eventual total or partial replacement by renewable and sustainable energy sources are highly desirable to decrease emissions of CO<sub>2</sub> and other greenhouse gases causing global warming. Because of this, current research efforts in catalysis are focused on the development of economically and energy-efficient processes for the production of sustainable fuels from renewable sources. In this sense, lignocellulosic biomass and organic waste have attracted attention for the production of clean biofuels capable to substitute or supplement fossil fuels.<sup>[2]</sup> Bio-oil is the main product obtained from lignocellulosic biomass through the quick pyrolysis process. The drawback of this bio-oil is a high oxygen content (35–40 wt%), which gives it low chemical stability and thermal value. The bio-oil derived from lignin consists mainly of aromatic compounds with hydroxy (–OH) and methoxy (–OCH<sub>3</sub>) substituents, such as anisole, phenol, guaiacol, catechol, syringol, isoeugenol, among others.<sup>[2]</sup> The hydrodeoxygenation (HDO) catalytic process is frequently used to reduce the oxygen content in bio-oil by the reaction with hydrogen, improving its stability and fuel properties. In the case of lignin-derived bio-oil, oxygen is removed in the form of water or methanol.<sup>[3]</sup>

Different supported solid catalysts have been tested for HDO: transition metal salts (sulfides, phosphides, carbides,

etc.), as well as reduced transition (Ni, Cu, Co, etc.) or noble (Pt, Pd, Rh, etc.) metals.<sup>[2]</sup> Noble metals are known to be effective for hydrogen activation under mild reaction conditions. Although the drawback of noble metals is the high cost, it was demonstrated recently that they can be used in catalytic processes with economic benefits.<sup>[4]</sup> In contrast, transition metals are abundant and less expensive. Among noble and non-noble metals, Pt and Ni catalysts have attracted significant attention in recent years for the HDO of biomass-derived chemicals.<sup>[5–14]</sup> Thus, Pt/SiO<sub>2</sub> catalysts with different particle size of Pt were used in the valorization of lignin into aromatic chemicals such as benzene, toluene, and xylenes (BTX).<sup>[5]</sup> Physically mixed Pt/AC and HZSM-5 catalysts<sup>[6]</sup> and bifunctional Pt catalysts supported on a zeolite-binder matrix<sup>[7]</sup> were investigated in the HDO of isoeugenol giving good results. Ni/γ-Al<sub>2</sub>O<sub>3</sub> catalysts also showed good activity in bio-oil upgrading.<sup>[8]</sup> Ni/SBA-15 and Ni/SiO<sub>2</sub> catalysts were tested in m-cresol HDO under atmospheric pressure<sup>[9]</sup> and in anisole HDO under 40 bar H<sub>2</sub> pressure.<sup>[10]</sup> In both works, the effect of Ni particle size on the activity and product distribution was observed. Large Ni nanoparticles promoted hydrogenation reactions, while small Ni nanoparticles exhibited high activity for C–O bond cleavage. Ni catalysts supported on Al-MCM-41 showed high activity and selectivity in HDO of anisole to cyclohexane.<sup>[11]</sup> Ni/Beta bifunctional catalysts were studied in the HDO of waste biomass for selective production of BTX compounds<sup>[12]</sup> and in methyl laurate HDO to bio-jet fuel.<sup>[13]</sup> Nickel nanoparticles supported on HZSM-5 catalysts showed exceptionally high selectivity, good stability, tolerance for impurities, and excellent recyclability in HDO of

To the memory of Elena Klimova.

lignin-related model compounds.<sup>[14,15]</sup> The above mentioned works<sup>[5–14]</sup> were published in 2023, showing that the development of novel supported metal catalysts for HDO is a hot topic. On the other hand, bimetallic NiPt catalysts are much less explored in HDO. In the year 2023, only two publications were found, where Pt–Ni bimetallics confined in a hierarchical ZSM-5 zeolite were tested in the HDO of phenolics with high yield of cyclohexane<sup>[16]</sup> and Ni–Pt catalysts supported on activated carbon were used for the hydrotreatment of guaiacol.<sup>[17]</sup> Regarding the supports commonly used for the preparation of HDO catalysts, conventional supports such as Al<sub>2</sub>O<sub>3</sub>, SiO<sub>2</sub>, TiO<sub>2</sub>, and carbon, mesoporous ordered materials (MCM-41, SBA-15, etc.) and microporous zeolites (HY, USY, H-Beta, HZSM-5, etc.) can be mentioned.<sup>[2,5–18]</sup>

In the present work, a comparison of Ni, Pt, and NiPt catalysts supported on SBA-15 silica was performed in the hydrodeoxygenation of anisole as a representative model compound of lignin-derived pyrolysis bio-oil. The catalysts were characterized in their oxide and reduced forms in order to inquire into the effect of platinum addition on the characteristics of Ni species at different steps of catalyst preparation. The objective of this work was to compare the behavior of mono- and bimetallic catalysts of a different metal nature (noble vs. non-noble) in hydrodeoxygenation, to prove if there is any synergy between the two selected metals and to gain a better understanding of the improved behavior of the bimetallic NiPt/SBA-15 catalyst.

## Materials and methods

### Synthesis of SBA-15 support

The mesoporous SBA-15 support was synthesized by the hydrothermal method described by Zhao et al.<sup>[18]</sup> Tetraethyl orthosilicate (TEOS, Aldrich) was used as the silica source and triblock copolymer EO<sub>20</sub>-PO<sub>70</sub>-EO<sub>20</sub> ( $M_{av}$  = 5800 g/mol, Aldrich) as the templating agent. The nominal molar ratio of the chemicals used in the synthesis was 1TEOS:0.017P123:5.9 5HCl:1.71H<sub>2</sub>O. The hydrothermal treatment was performed first upon stirring at 35 °C (20 h) and then without stirring at 100 °C (24 h). The obtained solid product was washed with deionized water and air-dried at room temperature. The calcination step was performed in static air at 550 °C for 6 h.

### Preparation of Ni, Pt, and NiPt catalysts

Mono- and bimetallic catalysts supported on SBA-15 were prepared by the conventional incipient wetness (co-)impregnation technique using aqueous solutions of nickel nitrate (Ni(NO<sub>3</sub>)<sub>2</sub>·6H<sub>2</sub>O, Aldrich) and hexachloroplatinic acid (H<sub>2</sub>PtCl<sub>6</sub>·6H<sub>2</sub>O, Aldrich) precursors. The theoretical loadings of metals in the catalysts were 5 wt% of Ni and 1 wt% of Pt. After the impregnation, the catalysts were dried at room temperature for 24 h, then at 100 °C for 12 h and calcined at 500 °C for 2 h in static air atmosphere. The prepared catalysts were labeled as Ni/SBA-15, Pt/SBA-15, and NiPt/SBA-15.

## Characterization

The SBA-15 support and prepared catalysts were characterized by N<sub>2</sub> physisorption, small- and wide-angle X-ray diffraction (XRD), temperature-programmed reduction (TPR), scanning electron microscopy with energy-dispersive X-ray spectroscopy (SEM–EDX), and transmission electron microscopy (TEM).

N<sub>2</sub> adsorption–desorption isotherms were obtained with a Micromeritics ASAP 2020 automatic analyzer at liquid N<sub>2</sub> temperature (– 197.5 °C). The samples were previously degassed at 270 °C for 10 h. Specific surface areas were calculated by the Brunauer–Emmett–Teller method ( $S_{BET}$ ). The total pore volume ( $V_p$ ) was determined by nitrogen adsorption at a relative pressure of 0.98 and pore size distributions were obtained from the adsorption and desorption isotherms by the Barrett–Joyner–Halenda (BJH) method. The reported mesopore diameters ( $D_{pads}$  and  $D_{pdes}$ ) were determined as the maxima of the corresponding pore size distributions. The micropore area ( $S_{\mu}$ ) was estimated using the correlation of t-Harkins & Jura (t-plot method).

Powder XRD measurements were performed on a Siemens D5000 diffractometer, using CuK $\alpha$  radiation ( $\lambda$  = 1.5406 Å) and a goniometer speed of 1° (2 $\theta$ ) per minute. The wide-angle XRD patterns of the samples were recorded from 3° to 80° (2 $\theta$ ). This technique was used for the characterization of calcined and reduced catalysts. The small-angle XRD patterns recorded from 0.6° to 5° (2 $\theta$ ) were obtained on a Bruker D8 Advance diffractometer using small divergence and scattering slits of 0.05°. The  $a_0$  unit-cell parameter of SBA-15-type materials was estimated from the position of the (100) diffraction line as  $a_0 = 2\sqrt{3} \times d_{100}$ . Pore wall thickness,  $\delta$ , was assessed by subtracting adsorption pore diameter ( $D_{pads}$ ) from the unit-cell parameter ( $a_0$ ).

TPR characterization was performed in a Micromeritics AutoChem II 2920 automatic analyzer equipped with a thermal conductivity detector. The catalysts (50 mg) were pre-treated at 400 °C for 2 h in air and then cooled to room temperature under an Ar stream. The consumption of H<sub>2</sub> was recorded from 25 to 1000 °C upon a heating rate of 10 °C/min in a stream of H<sub>2</sub>/Ar mixture (10/90 mol/mol, 50 mL/min flow).

The chemical composition of the catalysts was estimated by a SEM–EDX analysis, using a JEOL 5900 LV microscope with OXFORD ISIS equipment.

Characterization of metal nanoparticles in the reduced catalysts was performed by TEM. TEM images were obtained using a JEOL 2010 microscope (resolving power 1.9 Å at 200 kV). The solids were ultrasonically dispersed in heptane and the suspension was collected on carbon coated grids. The size of about 500 metal particles observed in different parts of various images of the reduced catalysts was determined and used to obtain a frequency histogram of the particle size. Scanning-transmission electron microscopy (STEM) in high-angle annular dark-field (HAADF) mode was performed in a

Cs-corrected JEOL ARM-200F electron microscope located at Laboratorio Universitario de Microscopía Electrónica (LUME-UNAM, RRID:SCR\_024400), operated at 200 keV. Energy-dispersive X-ray spectroscopy (EDS) was carried out with an Oxford AZtecTEM detector.

### Hydrodeoxygenation of anisole

Prior to the catalytic activity tests, the catalysts were reduced ex-situ in a U-shaped glass flow reactor at 400 °C for 4 h, under a stream of H<sub>2</sub>/Ar (70:30 mol:mol) at atmospheric pressure. The hydrodeoxygenation of anisole was performed in a 300 mL stainless steel batch reactor (Parr), with a model solution of 0.37 M of anisole (Aldrich, 99%) in hexadecane (Aldrich, 99%). In every activity test, 50 mL of anisole solution and 0.1 g of reduced catalyst were used. The reaction was performed at 280 °C and 7.3 MPa total pressure for 6 h upon constant mechanical stirring (500 rpm). Aliquots of the reaction mixture were taken every 15 min during the first hour, every 30 min during the second hour and then hourly until the end of the reaction. The analysis of the aliquots was carried out in an Agilent 6890 gas chromatograph equipped with a flame ionization detector and a non-polar methyl siloxane capillary column HP-1 (50 m × 0.32 mm inner diameter and 0.52 μm film thickness). Product identification was performed on an Agilent 7890A GC system equipped with 5975C MS detector. The catalytic activity was determined by measuring anisole concentrations at different reaction times. The conversion of anisole ( $X_{AN}$ ) was calculated as shown in Eq. 1, where  $C_{(AN)0}$  is the initial anisole concentration in the reaction mixture and  $C_{AN}$  is the concentration of anisole at different reaction times  $t$  (h).

$$X_{AN} = \frac{C_{(AN)0} - C_{AN}}{C_{(AN)0}} \times 100 \% \quad (1)$$

Selectivity to cyclohexane ( $S_{CHA}$ ) was defined as CHA content (%) in the reaction mixture.

## Results and discussion

### Support and catalyst characterization

The chemical composition of the prepared catalyst was determined by SEM–EDX. The catalysts have real metal loadings close to the theoretically expected ones (Table 1). Figure 1(a) shows distributions of metal species in monometallic Ni/SBA-15 and Pt/SBA-15 and bimetallic NiPt/SBA-15 catalysts. All the metals are well and homogeneously dispersed without forming large agglomerates. It seems that the dispersion of both metals (Ni and Pt) is better in the bimetallic NiPt catalyst.

The Fig. 1(b) shows nitrogen adsorption–desorption isotherms of the SBA-15 support and calcined catalysts, as well as corresponding pore size distributions. All the isotherms are of Type IV corresponding to mesoporous materials, with a H1 hysteresis loop pointing out to the presence of nearly cylindrical pore channels. Both isotherms and hysteresis loops are characteristic of the SBA-15 materials. The textural characteristics of the prepared SBA-15 support and mono- and bimetallic catalysts are shown in Table 1. The SBA-15 material exhibited the highest specific surface area (722 m<sup>2</sup>/g) and pore volume (1.23 cm<sup>3</sup>/g), while the catalysts showed decreased surface areas (595 to 668 m<sup>2</sup>/g) and pore volumes (0.99 to 1.13 cm<sup>3</sup>/g) due to the incorporation of non-porous metal species and some pore blocking. Adsorption and desorption pore diameters of the starting SBA-15 support suffered only slight changes in the mono- and bimetallic catalysts. Therefore, the pristine pore structure of the SBA-15 support was maintained in the catalysts after metal deposition by the incipient wetness impregnation technique. Additionally, it can be noted that  $D_{Pads}$  and  $D_{Pdes}$  show about 2 nm difference in the support and calcined catalysts (Fig. 1(b) and Table 1) indicating that in all the samples, mesopores have somewhat different internal and pore-mouth (entrance) diameters.

Figure 1(c) (left side chart) shows the small-angle diffractograms, 0.6°–3.0° ( $2\theta$ ), of the SBA-15 support and catalysts. The SBA-15 support exhibits well-defined diffractions at 0.9, 1.5° and 1.75° ( $2\theta$ ) typical of the two-dimensional hexagonal

**Table 1.** Chemical composition, textural and structural characteristics of the support and catalysts, and catalytic activity at different steps of anisole hydrodeoxygenation.

Sample	Real metal loading (wt%) <sup>a</sup>	Textural <sup>b</sup> and structural <sup>c</sup> characteristics							Activity <sup>d</sup>	
		$S_{BET}$ (m <sup>2</sup> /g)	$V_p$ (cm <sup>3</sup> /g)	$S_\mu$ (m <sup>2</sup> /g)	$D_{Pads}$ (nm)	$D_{Pdes}$ (nm)	$a_0$ (nm)	$\delta$ (nm)	$k_1$ (h <sup>-1</sup> )	$k_2$ (h <sup>-1</sup> )
SBA-15	–	722	1.23	51	8.8	6.7	11.7	2.9	–	–
Ni/SBA-15	5.04	599	1.04	53	8.5	6.6	11.3	2.8	1.56	0.08
Pt/SBA-15	0.83	668	1.13	55	8.8	6.7	11.3	2.5	0.61	0.04
NiPt/SBA-15	5.05 (Ni), 1.01 (Pt)	595	0.99	51	8.6	6.6	11.3	2.7	2.54	0.20

<sup>a</sup>Determined by SEM–EDX analysis. Nominal metal loadings in the catalyst: 5 wt% of Ni and 1 wt% of Pt.

<sup>b</sup> $S_{BET}$ , specific surface area;  $V_p$ , total pore volume;  $S_\mu$ , micropore area;  $D_{Pads}$  and  $D_{Pdes}$ , mesopore diameters determined from the adsorption and desorption isotherms, respectively.

<sup>c</sup> $a_0$ , unit-cell parameter;  $\delta$ , pore wall thickness of SBA-15 materials.

<sup>d</sup>Pseudo-first order reaction rate constants:  $k_1$  for the hydrogenation of the aromatic ring of anisole and  $k_2$  for the hydrogenolysis of C–O bond in cyclohexyl methyl ether intermediate.



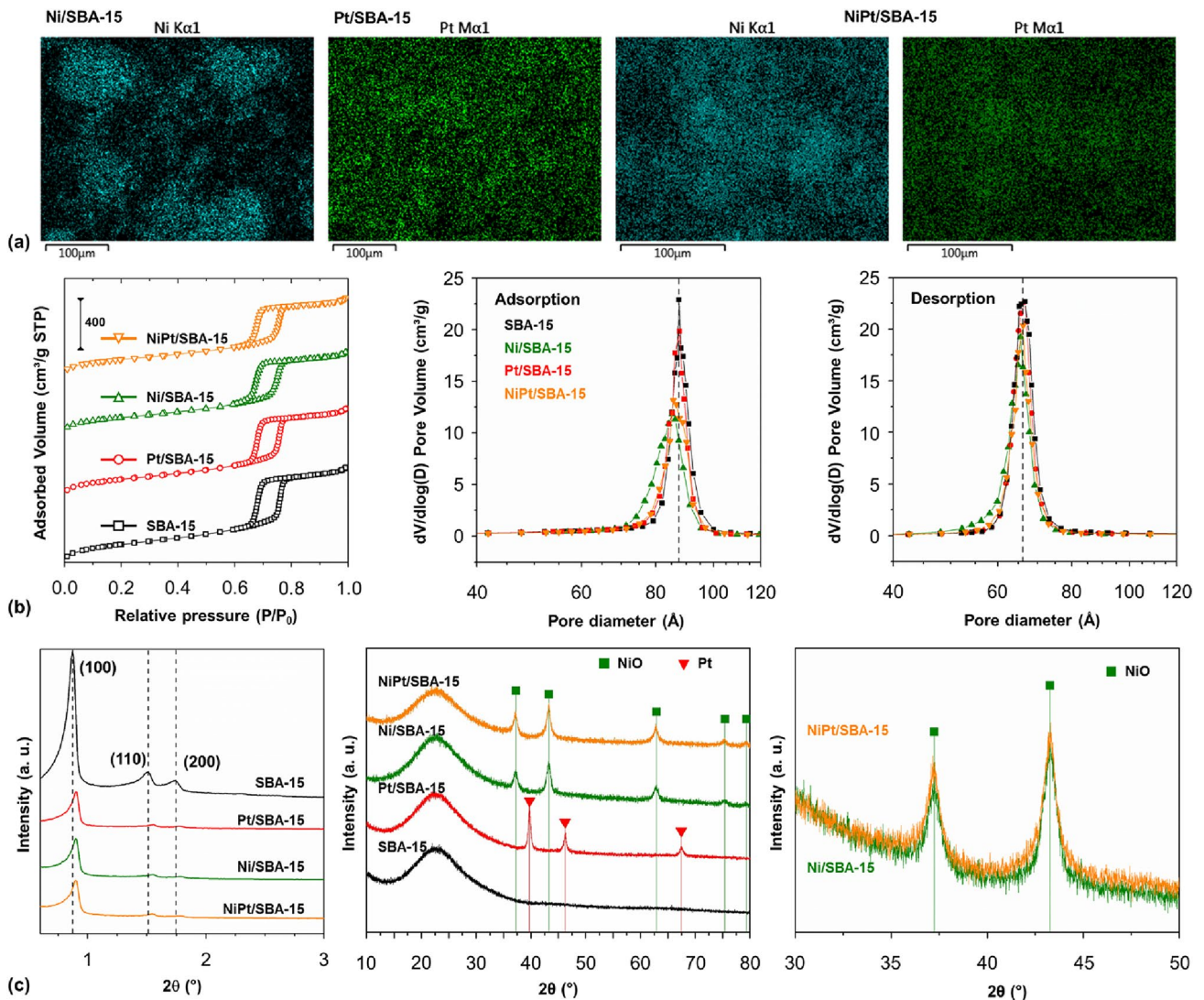


**Figure 1.** (a) Elemental mappings of calcined mono- and bimetallic catalysts; (b)  $N_2$  adsorption–desorption isotherms and pore size distributions of the support and calcined catalysts; (c) small-angle and wide-angle X-ray diffraction patterns of the support and calcined catalysts.

$p6mm$  pore structure, which are associated with the (1 0 0), (1 1 0), and (2 0 0) planes, respectively. In this pore structure, one central pore is surrounded by other six pores of the same size. These characteristic diffractions are also present in the patterns of the calcined mono- and bimetallic catalysts. However, the intensity of the (1 0 0) signal was lower for the catalysts than for the SBA-15 support, which could be due to some pore blocking of the support's mesopore structure by the deposited metal species and a decrease in the long-order pore arrangement. This confirms that the characteristic hexagonal arrangement of the SBA-15 pore structure was maintained in the catalysts even after the impregnation of metal precursors and calcination treatment. The pore wall thickness was determined using the cell parameter  $a_0$  calculated based on the position of the  $d_{100}$  interplanar distance and the  $D_{Pads}$  pore size obtained

from nitrogen adsorption isotherms. According to Table 1, the calcined catalysts showed pore wall thickness ( $\delta$ ) similar to that of the SBA-15 support. This means that the mechanical and thermal resistance properties of the support were maintained in the catalysts.

Figure 1(c) (central chart) shows the results of powder X-ray diffraction analysis of the SBA-15 support and calcined catalysts in the  $10^\circ$ – $80^\circ$  ( $2\theta$ ) interval. The SBA-15 support shows a broad signal between  $15^\circ$  and  $35^\circ$  ( $2\theta$ ) corresponding to amorphous silica. The same broad signal of the support is also observed in the diffraction patterns of the calcined catalysts. In addition, five new diffraction signals were observed for Ni/SBA-15 and NiPt/SBA-15 catalysts at  $37.25^\circ$ ,  $43.28^\circ$ ,  $62.98^\circ$ ,  $75.63^\circ$ , and  $79.39^\circ$  ( $2\theta$ ). These signals correspond well to the (111), (200), (220), (311), and (222) planes of the

cubic (*Fm-3m*) crystalline phase card of nickel(II) oxide (NiO, JCPDS-ICDD 01-071-1179). For the Pt/SBA-15 catalyst, characteristic signals of cubic (*Fm-3m*) crystalline phase of metallic platinum (Pt, JCPDS-ICDD card 00-004-0802) were detected at 39.77°, 46.31°, and 67.52° ( $2\theta$ ). These signals were assigned to the (111), (200), and (220) planes, respectively. An interesting finding is that no signals of metallic Pt phase were detected in the bimetallic NiPt/SBA-15 sample. This means that the dispersion of Pt was significantly improved in the presence of NiO in the bimetallic catalyst. However, we did not find any evidence of the formation of any mixed phase between Pt and NiO in the calcined NiPt/SBA-15 sample. The more intense signals of the NiO phase (37.25° and 43.28° ( $2\theta$ )) did not show any shift in the presence of Pt compared to the positions of these signals in the Ni/SBA-15 catalyst, Fig. 1(c) right side chart.

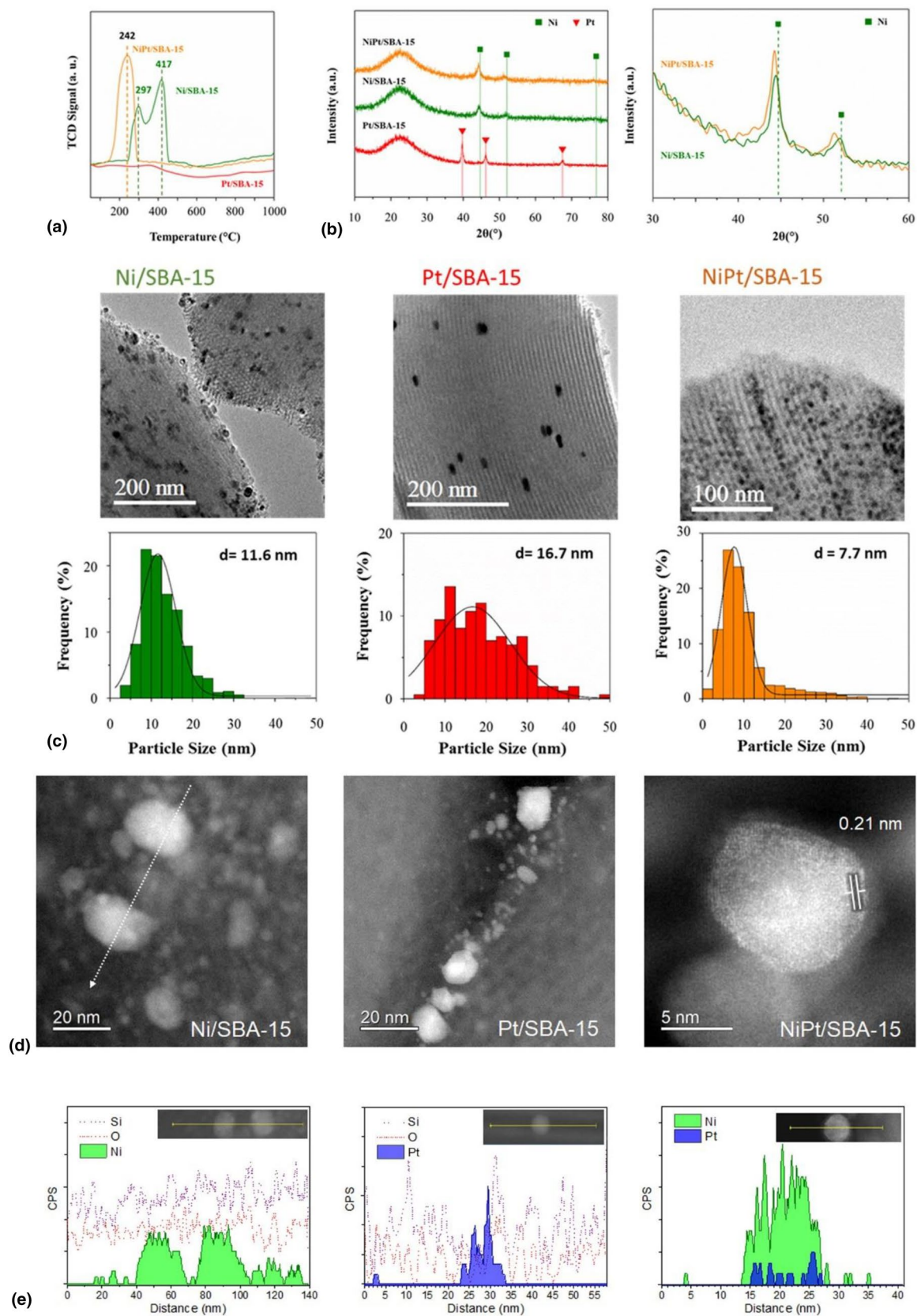
TPR profiles of the calcined mono- and bimetallic Ni and Pt catalysts are shown in Fig. 2(a). Reduction of NiO takes place just in one step ( $\text{Ni}^{2+}\text{O} + \text{H}_2 \rightarrow \text{Ni}^0 + \text{H}_2\text{O}$ ). Therefore, the presence of two main reduction peaks with maxima at 297 and 417 °C in the reduction profile of the calcined Ni/SBA-15 catalyst points out to the coexistence of two different nickel oxide species in this catalyst. The lower temperature reduction peak (297 °C) could be ascribed to the reduction of free NiO species, which are in weak interaction with the silica support. These could be crystalline NiO species detected by XRD and, according to their size determined using the Scherrer equation (~13.6 nm), they should be located on the external surface of the SBA-15 support. The second reduction peak (417 °C) can be attributed to the NiO species in a stronger interaction with the silica support. These could be smaller NiO species confined inside the SBA-15 mesopores. No reduction signals were detected for the Pt/SBA-15 catalyst. This is in line with the XRD observations, where the presence of only metallic platinum was found. Both XRD and TPR characterizations hint at the reduction of  $\text{PtO}_x$  species during the synthesis of this catalyst, probably, in the calcination step. For the bimetallic NiPt/SBA-15 catalyst, only one reduction peak with a maximum at 242 °C was detected, Fig. 2(a). This result indicates that in presence of platinum, the reduction of NiO species occurs at a significantly lower temperature. In addition, the reduction of just one type of NiO species was observed in the calcined bimetallic NiPt/SBA-15 catalyst. However, from the TPR results it is not clear if these NiO species are located inside or outside the SBA-15 pores. A similar decrease in the reduction temperature of the NiO was reported recently for the Ni–Pt catalysts supported on activated carbon (AC)<sup>[17]</sup> and for the Pt/Ni catalysts supported on SBA-15 and Al-SBA-15.<sup>[19]</sup> The promoting effect of Pt on the reduction temperature of nickel oxide species was ascribed to a synergistic effect with a potential hydrogen spillover from Pt sites to NiO species in bimetallic systems affecting the formation of Ni nanoparticles.<sup>[17,19,20]</sup>

Figure 2(b) shows the XRD patterns of the catalysts reduced at 400 °C for 4 h. For the Ni/SBA-15 and NiPt/SBA-15 catalysts, no signals corresponding to the NiO crystalline phase were observed after reduction. Three new reflections were

observed at 44.75°, 52.10°, and 76.81° ( $2\theta$ ) corresponding to the (111), (200), and (220) planes of the crystalline cubic phase of metallic nickel ( $\text{Ni}^0$ , JCPDS-ICDD card 01-071-4655). The monometallic Pt/SBA-15 catalyst shows the same diffraction peaks as the calcined catalyst, since Pt was reduced prior to the reduction treatment. For the bimetallic NiPt/SBA-15 catalyst, signals of the crystalline phase of metallic Pt were not observed. However, a slight shift of the diffraction signals of metallic  $\text{Ni}^0$  toward smaller  $2\theta$  degrees was detected [Fig. 2(b), right chart]. This could be due to the incorporation of larger Pt atoms into the crystalline structure of  $\text{Ni}^0$ . This is possible according to the Effective-Medium Theory (EMT),<sup>[21]</sup> since the energies of segregation and surface mixing between Pt and Ni allow non-segregated mixing of Pt and Ni. Therefore, evidence of the incorporation of Pt into the Ni matrix was found.

The reduced mono- and bimetallic Ni, Pt, and NiPt catalysts were examined by transmission electron microscopy (TEM) to observe location and size of metal nanoparticles. Figure 2(c) shows the TEM images and particle size distributions of the prepared catalysts. In all the images, the characteristic ordered mesopore structure of the SBA-15 support can be observed. Metallic nanoparticles are seen as dark gray-black spots. The reduced Ni/SBA-15 catalyst showed a broad particle size distribution (2.5 to 32.5 nm) with an average particle size of 11.6 nm. Some Ni nanoparticles (small particles with a size below the pore size of the SBA-15 support, Table 1) could be located inside the support's mesopores. However, the majority of the Ni particles have a size above 10 nm and these large metal nanoparticles can be observed on the external surface of the SBA-15. The reduced Pt/SBA-15 catalyst showed even broader metal Pt particle size distribution (from 5 to 40 nm), being the average particle size equal to 16.7 nm. In this case, some of the observed large metal particles may be located on the external surface of the SBA-15 support. However, some metal particles seem to have cylindrical shape and are aligned along the support's mesopores, indicating the possibility of their location inside the mesopores blocking them. Resuming the above results, for the monometallic Ni and Pt catalysts, broad particle size distributions were obtained with the presence of metal nanoparticles of different sizes (heterogeneous distribution). Regarding the reduced bimetallic NiPt/SBA-15 catalyst, it presented a significantly narrower particle size distribution, where metal nanoparticles with size from 2.5 to 15 nm were predominant. The average particle size in this case was 7.7 nm. In addition, it can be clearly observed in Fig. 2(c) that nanoparticles of almost similar size are aligned inside the cylindrical mesopores of the support. An increase in the dispersion of metal nanoparticles in the bimetallic NiPt catalyst compared to the monometallic ones is in line with previous report,<sup>[17]</sup> where the formation of uniform Ni–Pt nanoparticles was detected in the Ni–Pt/AC catalysts.

HAADF imaging and EDS analysis was performed to corroborate the local composition of the reduced catalysts. Figure 2(d) shows the images of the monometallic catalysts. It can be seen in detail the size dispersion of the particles. In the



**Figure 2.** (a) TPR profiles of calcined catalysts; (b) wide-angle XRD patterns of reduced catalysts; (c) TEM micrographs and particle size distribution histograms of reduced mono- and bimetallic catalysts; (d) STEM images of reduced catalysts: Ni/SBA-15, Pt/SBA-15, and NiPt/SBA-15. (e) The corresponding EDS linescans. The presence of Ni and Pt is confirmed in the bimetallic nanoparticle.



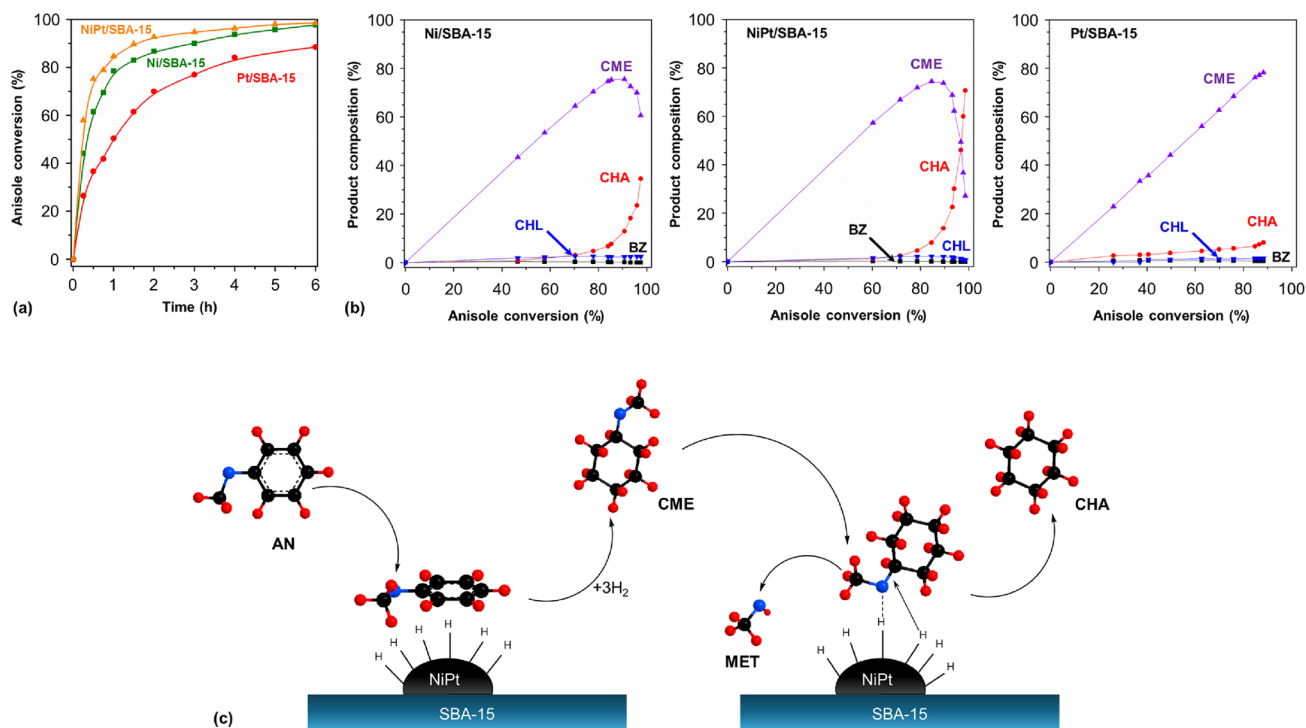
case of the NiPt/SBA-15 catalyst, a high-magnification image shows the nanoparticle structure. Platinum is well dispersed into the nickel structure of the particle, easily discernible by the high difference in contrast (Z contrast) between both elements. Lattice fringes were resolved, slightly dimmed by the SBA thickness. The measured lattice distance of 0.210 nm laid between the (111) planes of nickel or platinum (0.203 nm and 0.226 nm, respectively), indicates that Pt atoms incorporate into the face-centered cubic structure of nickel, forming an alloy. This is in agreement with the slight shift of the diffraction signals observed in the XRD pattern of this sample. Pt segregation is expected in this alloy, exposing Pt to the surface, which can enhance the catalytic activity.<sup>[22]</sup> Finally, EDS linescans confirmed the chemical composition of the monometallic and bimetallic catalysts, Fig. 2(e).

### Catalytic activity in the hydrodeoxygenation of anisole

Catalytic activity of the prepared catalysts was evaluated in the hydrodeoxygenation (HDO) of anisole (AN) at 280 °C and 7.3 MPa of H<sub>2</sub> total pressure. Figure 3(a) shows the anisole conversions obtained with the prepared catalysts. All the prepared catalysts were active in this reaction. The bimetallic NiPt/SBA-15 catalyst was the most active, followed by Ni/SBA-15 and then the Pt/SBA-15. These activity trends could be expected based on the results obtained for the reduced catalysts by TEM, Fig. 2(c). Smaller metal nanoparticles and, therefore,

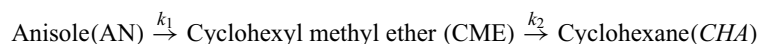
better dispersion of the catalytically active phase was observed for the bimetallic NiPt/SBA-15 catalyst compared to the monometallic samples. In addition, according to the results from TPR, Pt addition to the nickel catalyst promoted the reduction of nickel oxide species in the bimetallic NiPt/SBA-15 catalyst at a considerably lower temperature than in the Ni/SBA-15 analog. Finally, total metal loading in the bimetallic NiPt/SBA-15 catalyst (5 wt% Ni and 1 wt% Pt) was higher than in the monometallic Ni/SBA-15 (5 wt% Ni) and Pt/SBA-15 (1 wt% Pt) counterparts.

Figure 3(b) shows reaction product compositions obtained in the HDO of anisole with the synthesized Ni/SBA-15, Pt/SBA-15, and NiPt/SBA-15 catalysts. The following compounds were identified in the reaction mixture: cyclohexyl methyl ether (CME), cyclohexanol (CHL), benzene (BZ), cyclohexane (CHA), and methanol (MET). Methanol was not quantified because of its high volatility. According to the concentration profiles, the first three products (CME, CHL, and BZ) are intermediate products, while CHA is the final, hydrogenated and deoxygenated product of the hydrodeoxygenation of anisole. CME is the main intermediate product formed in a significant amount during the reaction (up to 75–80%). Another two intermediates (CHL and BZ) are formed in just small amounts (below 2–3%). Therefore, the reaction route involving these compounds may be ignored, and a simplified reaction scheme can be proposed for the hydrodeoxygenation of anisole with the studied Ni/SBA-15, Pt/SBA-15, and NiPt/SBA-15 catalysts,



**Figure 3.** (a) Conversions of anisole obtained with mono- and bimetallic catalysts at 280 °C and 7.3 MPa total pressure; (b) reaction product compositions obtained over Ni/SBA-15, NiPt/SBA-15, and Pt/SBA-15 catalysts, and (c) proposed reaction mechanism of the HDO of anisole. AN anisole, CHA cyclohexane, CME cyclohexyl methyl ether, CHL cyclohexanol, BZ benzene, MET methanol.

Fig. 3(c). The first step of the above reaction mechanism corresponds to the hydrogenation of the aromatic ring of anisole leading to the formation of CME. In the second step, the CME intermediate is deoxygenated into cyclohexane. This reaction mechanism represents a system of two consecutive irreversible pseudo-first order reactions:



Regarding hydrogen, both reactions can be considered of pseudo-order zero for this reactant due to the high  $\text{H}_2$  pressure used in the catalytic activity tests. According to the above mechanism, two reaction rate constants were estimated:  $k_1$  for hydrogenation of anisole and  $k_2$  for hydrodeoxygenation (demethoxylation) of CME. For these calculations, kinetic equations (Eqs. 2–4) were considered and a curve-fitting method was employed for experimentally obtained data for AN, CME, and CHA concentrations ( $C_{\text{AN}}$ ,  $C_{\text{CME}}$ , and  $C_{\text{CHA}}$ , respectively, being  $C_{(\text{AN})0}$  the initial anisole concentration).<sup>[23]</sup>

$$C_{\text{AN}} = C_{(\text{AN})0} e^{-k_1 t} \quad (2)$$

$$C_{\text{CME}} = \frac{k_1 C_{(\text{AN})0}}{k_2 - k_1} \left[ e^{-k_1 t} - e^{-k_2 t} \right] \quad (3)$$

$$C_{\text{CHA}} = \frac{C_{(\text{AN})0}}{k_2 - k_1} \left[ k_2 \left( 1 - e^{-k_1 t} \right) - k_1 \left( 1 - e^{-k_2 t} \right) \right] \quad (4)$$

Obtained values of kinetic constants are shown in Table 1 (last two columns). It can be noted that both reaction rate constants,  $k_1$  and  $k_2$ , change in the following order: Pt/SBA-15 < Ni/SBA-15 < NiPt/SBA-15, being the bimetallic NiPt catalyst the most active for both reactions (hydrogenation and demethoxylation). In addition, it was found that the combination of two metals (Ni and Pt) in one bimetallic catalyst resulted in greater values of the obtained  $k_1$  and  $k_2$  constants than those obtained as the sum of the corresponding constants of monometallic catalysts. For example,  $k_1$  equal to  $2.54 \text{ h}^{-1}$  for the NiPt/SBA-15 catalyst is larger than the sum of the  $k_1$  constants of the Ni/SBA-15 and Pt/SBA-15 which is  $2.17 \text{ h}^{-1}$  (about 20% difference). Ever more notorious was the difference observed between the  $k_2$  value of the NiPt catalyst ( $0.20 \text{ h}^{-1}$ ) and the sum of  $k_2$  of monometallic analogs ( $0.12 \text{ h}^{-1}$ , more than 60% difference). The above observations evidence the synergistic effect between Ni and Pt components of the bimetallic catalyst on its catalytic activity. Another proof of Ni and Pt cooperation in the NiPt/SBA-15 catalyst is its improved selectivity for the final CHA product, Fig. 3(b). The amount of CHA obtained with the NiPt catalyst at 6 h reaction time is about 75%, while only ~10% of CHA was obtained with the Pt/SBA-15 catalyst and 35% with the Ni/SBA-15 catalyst at the same reaction time. This result could be ascribed to the incorporation of Pt into the reduced Ni nanoparticles forming a Ni-Pt alloy and the modification of the electronic properties of the latter making easier the rupture of the C-O bond of CME and its hydrodeoxygenation to CHA.

Finally, it can be noted in Fig. 3(b) for the Ni/SBA-15 and NiPt/SBA-15 catalysts that the formation of the final CHA product starts at high anisole conversions (above 70%). At lower anisole conversions, hydrogenolysis of the C-O bond in the CME intermediate is inhibited. This could mean that hydrogenation and demethoxylation reactions take place on the same active

phase, namely metal nanoparticles, and that both molecules AN and CME compete for the same active sites, being AN easier to be adsorbed and reacted than CME. Such an assumption seems to be reasonable considering that AN adsorption could take place in a mode, where the molecule is oriented parallel to the metal surface with the participation of  $\pi$ -electrons of the conjugated six-membered aromatic ring of anisole. On the other hand, the C-O bond rupture in the CME intermediate comprises the coordination of an oxygen atom to the surface of the metal nanoparticle just through a free pair of electrons of the oxygen atom, making this adsorption less strong.

The above activity and selectivity results obtained in the present study are in line with previous literature reports. Thus, it was shown for the HDO of dibenzofuran in water that bimetallic Ni/M (M = Ru, Rh, and Pd) catalysts inherited the advantages of both components, namely, the noble metal increased the hydrogenation activity of the catalyst, while Ni modified the selectivity of the noble metal to favor the C-O bond cleavage.<sup>[24]</sup> A similar effect was also observed for the unsupported  $\text{Ni}_{86}\text{Pt}_{14}$  catalyst in the HDO of dibenzofuran.<sup>[25]</sup> The high catalytic activity and selectivity of the  $\text{Ni}_{86}\text{Pt}_{14}$  catalysts was ascribed to its structural characteristics (a smaller metal particle size compared to the corresponding single metal catalysts and Ni enrichment in the catalyst's surface). In work,<sup>[17]</sup> strong Ni-Pt interactions were detected by XPS in Ni-Pt catalysts supported on activated carbon (AC). Distinctive electronic features of Ni-Pt/AC were also revealed, which were favorable for the transformation of guaiacol to cyclohexanol with increasing Pt loading. In addition, Pt enhanced catalyst stability by inhibiting the oxidation of Ni sites and mitigating Ni-Pt phase sintering. Bimetallic NiPt catalysts supported on hierarchical ZSM-5 materials were investigated in a gas-phase hydrodeoxygenation, transalkylation and dealkylation reaction of model lignin derivative molecules for phenol production.<sup>[26]</sup> Among the studied catalysts, 10Ni1Pt/Z-h showed the highest activity and selectivity for phenol production, which was attributed to the additive effect of Pt related to the increase in the metal dispersion and enhancement of NiO reducibility.

## Conclusion

Mono- and bimetallic catalysts supported on SBA-15 silica (Ni/SBA-15, Pt/SBA-15, and NiPt/SBA-15) were successfully prepared, characterized, and tested in the HDO of anisole. The bimetallic NiPt/SBA-15 catalyst showed smaller size of the



reduced metallic particles and better dispersion than the corresponding monometallic analogs, which can be due to the formation of a Ni-Pt alloy. Addition of Pt to the Ni catalyst supported on SBA-15 resulted in a notorious decrease in the temperature of reduction of NiO that can be attributed to easy activation of H<sub>2</sub> on Pt atoms at low temperature and hydrogen spillover to NiO species. The bimetallic NiPt/SBA-15 catalysts showed higher activity and selectivity to deoxygenated products than the corresponding monometallic catalysts. A synergistic effect between Ni and Pt species observed in the bimetallic NiPt/SBA-15 catalyst was attributed to the formation of a Ni-Pt alloy.

## Acknowledgments

D.E. Pérez-Estrada acknowledges Consejo Nacional de Humanidades, Ciencias y Tecnologías (CONAHCYT, México) for his Ph. D. scholarship through CVU 854325. The authors thank C. Salcedo Luna, A. Morales Espino, I. Puente Lee, and J. Romero for technical assistance with XRD and SEM/TEM characterizations.

## Author contributions

DEPE and MASV performed the experiments; DEPE, LHMC and ASM were responsible for data analysis and visualization; DEPE wrote the original draft of the manuscript; RMC performed STEM data analysis and writing, TEK wrote, reviewed and edited the manuscript; TEK was responsible for funding acquisition, supervision and project administration; all authors contributed to the general discussion.

## Funding

Financial support from Dirección General de Asuntos de Personal Académico – Universidad Nacional Autónoma de México, DGAPA-UNAM, México [grants IN-114121 and IA-106623] is gratefully acknowledged.

## Data availability

Data will be made available upon reasonable request.

## Declarations

### Conflict of interest

The authors declare no conflict of interest.

## Open Access

This article is licensed under a Creative Commons Attribution 4.0 International License, which permits use, sharing, adaptation, distribution and reproduction in any medium or format, as long as you give appropriate credit to the original author(s) and the source, provide a link to the Creative Commons licence, and

indicate if changes were made. The images or other third party material in this article are included in the article's Creative Commons licence, unless indicated otherwise in a credit line to the material. If material is not included in the article's Creative Commons licence and your intended use is not permitted by statutory regulation or exceeds the permitted use, you will need to obtain permission directly from the copyright holder. To view a copy of this licence, visit <http://creativecommons.org/licenses/by/4.0/>.

## References

- G.W. Huber, S. Iborra, A. Corma, Synthesis of transportation fuels from biomass: chemistry, catalysts, and engineering. *Chem. Rev.* **106**, 4044–4098 (2006)
- M.E. Martínez-Klimov, P. Mäki-Arvela, D.Y. Murzin, Catalysis for production of jet fuel from renewable sources by hydrodeoxygenation and hydrocracking. *Catalysis* **33**, 181–213 (2021)
- P.M. Mortensen, J.D. Grunwaldt, P.A. Jensen, K.G. Knudsen, A.D. Jensen, A review of catalytic upgrading of bio-oil to engine fuels. *Appl. Catal. A* **407**, 1–19 (2011)
- A.A. Komarova, D.S. Perekalin, Noble metal versus abundant metal catalysts in fine organic synthesis: cost comparison of C-H activation methods. *Organometal.* **42**, 1433–1438 (2023)
- J. Marlowe, P.C. Ford, M.M. Abu-Omar, P. Christopher, Structure sensitivity in Pt-catalyzed hydrodeoxygenation of multi-oxygenated lignol model compounds. *Catal. Sci. Technol.* **13**, 5662–5678 (2023)
- V.S. Prabhudesai, R. Vinu, Hydrodeoxygenation of biomass-derived oxygenate mixtures over Pt/C and HZSM-5 mixed catalysts. *Topics Catal.* **66**, 405–419 (2023)
- M.E. Martínez-Klimov, P. Mäki-Arvela, Z. Vajglová, C. Schmidt, O. Yevdokimova, M. Peurla, N. Kumar, K. Eränen, D. Y. Murzin, Bifunctional Pt catalysts supported on a zeolite-binder matrix for the hydrodeoxygenation of isoeugenol for renewable jet fuel production. *Topics Catal.* **66**, 1296–1309 (2023)
- S. Jantasee, N. Rodtuk, W. Mens, C. Chaiya, Upgrading of soybean meal-derived bio-oil via hydrodeoxygenation over  $\gamma$ -Al<sub>2</sub>O<sub>3</sub>-supported monometallic and bimetallic catalysts. *Energy Rep.* **9**, 484–489 (2023)
- C.A. Teles, C. Ciotonea, A. Le Valant, C. Canaff, J. Dhainaut, J.-M. Clacens, F.B. Noronha, F. Richard, S. Royer, Optimization of catalyst activity and stability in the m-cresol hydrodeoxygenation through Ni particle size control. *Appl. Catal. B* **338**, 123030 (2023)
- P. Yan, X. Tian, E.M. Kennedy, M. Stockenhuber, Advanced in situ IR spectroscopy study of anisole hydrodeoxygenation over Ni/SiO<sub>2</sub> catalysts. *J. Catal.* **427**, 115102 (2023)
- L.H. Molina-Conde, A. Suárez-Méndez, D.E. Pérez-Estrada, T.E. Klimova, Mesoporous Ni/Al-MCM-41 catalysts for highly active and selective hydrodeoxygenation of anisole to cyclohexane. *Appl. Catal. A* **663**, 119313 (2023)
- O. Ismail, A. Hamid, L. Ali, T. Shittu, M.S. Kuttiyathil, M.Z. Iqbal, A. Khaleel, M. Altarawneh, Selective formation of fuel BXT compounds from catalytic hydrodeoxygenation of waste biomass over Ni-decorated beta-zeolite. *Bioresour. Tech. Rep.* **24**, 101616 (2023)
- T. Wang, W. Zhang, Y. Li, F. Li, J. Liu, L. Fan, J. Fu, X. Liu, Y. Lyu, Quantitative synergy between metal and acid centers over the Ni/Beta bifunctional catalyst for methyl laurate hydrodeoxygenation to bio-jet fuel. *Fuel Process. Tech.* **241**, 107602 (2023)
- Y.-H. Kang, J. Gao, X.-Q. Zhang, Y. Gao, Z.-H. Wang, Y.-J. Li, G.-H. Liu, X.-R. Ma, A.-M. Wang, J.-J. Bai, Z.-M. Zong, X.-Y. Wei, Synergistic effect of acidity and active phases for nickel nanoparticles supported HZSM-5 catalysts on lignin-related model compounds hydrodeoxygenation performance under mild conditions. *Ind. Crops Prod.* **198**, 116704 (2023)
- B. Saini, A.P. Tathod, J. Diwakar, S. Arumugam, N. Viswanadham, Nickel nano-particles confined in ZSM-5 framework as an efficient catalyst for selective hydrodeoxygenation of lignin-derived monomers. *Biomass Bioener.* **157**, 106350 (2022)

16. Y. Tian, L. Guo, C. Qiao, Z. Sun, Y. Yamauchi, S. Liu, Dynamics-driven tailoring of sub-nanometric Pt-Ni bimetallics confined in hierarchical zeolite for catalytic hydrodeoxygenation. *Appl. Catal. B* **336**, 122945 (2023)
17. W. Jin, J. Gandara-Loe, L. Pastor-Pérez, J.J. Villora-Picó, A. Sepúlveda-Escribano, R. Rinaldi, T.R. Reina, Guaiacol hydrotreatment in an integrated APR-HDO process: Exploring the promoting effect of platinum on Ni-Pt catalysts and assessing methanol and glycerol as hydrogen sources. *Renew. Energy* **215**, 118907 (2023)
18. D. Zhao, Q. Huo, J. Feng, B.F. Chmelka, G.D. Stucky, Nonionic triblock and star diblock copolymer and oligomeric surfactant syntheses of highly ordered, hydrothermally stable, mesoporous silica structures. *J. Am. Chem. Soc.* **120**, 6024–6036 (1998)
19. P. Sudhakar, A. Pandurangan, Pt/Ni wet impregnated over Al incorporated mesoporous silicates: a highly efficient catalyst for anisole hydrodeoxygenation. *J. Por. Mater.* **25**, 747–759 (2018)
20. M. El Doukkali, A. Iriondo, P.L. Arias, J. Requies, I. Gandarías, L. Jalowiecki-Duhamel, F. Dumeignil, A comparison of sol-gel and impregnated Pt or/and Ni based  $\gamma$ -alumina catalysts for bioglycerol aqueous phase reforming. *Appl. Catal. B* **125**, 516–529 (2012)
21. A. Christensen, A.V. Ruban, P. Stolze, K.W. Jacobsen, H.L. Skriver, J.K. Nørskov, Phase diagrams for surface alloys. *Phys. Rev. B* **56**, 5822–5834 (1997)
22. G. Guisbiers, R. Mendoza-Pérez, L. Bazán-Díaz, R. Mendoza-Cruz, J.J. Velázquez-Salazar, M. José-Yacamán, Size and shape effects on the phase diagrams of nickel-based bimetallic nanoalloys. *J. Phys. Chem. C* **121**, 6930–6939 (2017)
23. H.L. Pardue, Kinetic aspects of analytical chemistry. *Anal. Chim. Acta* **216**, 69–107 (1989)
24. J. Zhang, J. Teo, X. Chen, H. Asakura, T. Tanaka, K. Teramura, N. Yan, A series of NiM (M = Ru, Rh, and Pd) bimetallic catalysts for effective lignin hydrogenolysis in water. *ACS Catal.* **4**, 1574–1583 (2014)
25. P. Dong, G. Lu, C. Cai, Effective hydrodeoxygenation of dibenzofuran by a bimetallic catalyst in water. *New J. Chem.* **40**, 1605–1609 (2016)
26. M. Popova, Á. Szegedi, M. Oykova, H. Lazarova, N. Koseva, M.R. Mihályi, P. Shestakova, Selective production of phenol on bifunctional, hierarchical ZSM-5 zeolites. *Molecules* **26**, 3576 (2021)

**Publisher's Note** Springer Nature remains neutral with regard to jurisdictional claims in published maps and institutional affiliations.